Effect of Grain Size on the Fracture Behavior of Organic-Inorganic Halide Perovskite Thin Films for Solar Cells

Zhenghong Dai, Srinivas K. Yadavalli, Mingyu Hu, Min Chen, Yuanyuan Zhou, and Nitin P. Padture*

School of Engineering, Brown University, Providence, RI 02912, USA

For: Scripta Materialia (Manuscript No. SMM-20-414)

Abstract

Organic-inorganic halide perovskite (OIHP) thin films at the heart of the new perovskite solar cells (PSCs) are very brittle, limiting the mechanical reliability of PSCs. Here we show that fine-grained MAPbI₃ (prototypical OIHP) films with grain size (~290 nm) smaller than the typical film thickness (~500 nm) tend to fracture intergranularly, resulting in low toughness (0.41 J.m⁻²). In contrast, MAPbI₃/substrate interfacial fracture occurs in films with grains larger (~840 nm) than the film thickness, resulting in much higher toughness (1.14 J.m⁻²). Thus, coarse-grained OIHP films are deemed desirable for not only improved PSCs performance and stability but also mechanical reliability.

Keywords: halide perovskites; thin films; mechanical behavior; grain boundaries; solar cells

^{*} Corresponding author. Email address: nitin padture@brown.edu (N.P. Padture)

The record efficiency of perovskite solar cells (PSCs), incorporating thin films of organic-inorganic halide perovskite (OIHP) as light absorbers,[1-3] has rocketed from 3.8% in 2009 [4] to 25.2% in 2019,[5] rivalling silicon solar cells. The promise of low-cost, solution-processed PSCs with high efficiencies,[6] and their potential impact on the global renewable-energy landscape, is driving this effort worldwide. Also, the light-weight, thin-film nature of PSCs makes them uniquely suitable as flexible PVs for portable-power applications such as chargers, tents, backpacks, deployable rollups, drones, *etc.*[7-9] Furthermore, OIHPs are also useful in other potential applications such as light-emitting diodes, lasers, and detectors.[10]

The low formation energies of OIHPs makes it possible to solution-process them, at or near room temperature,[6] but it also makes them unstable.[11, 12] While significant progress has been made in improving the stability of OIHPs,[11, 12] any devices incorporating OIHPs will also need to be mechanically reliable if they are to operate satisfactorily for decades.[12-16] The mechanical stresses that the OIHPs within PSCs will need to endure include internal residual stresses, stresses arising from thermal excursions, and externally-applied stresses during manufacturing and service. Unfortunately, the low formation energies of OIHPs also makes them compliant (low Young's modulus, E), soft (low hardness, E), and brittle (low fracture toughness, E).[13-15, 17, 18, 19 20, 21]. For example, the prototypical OIHP — methylammonium lead triiodide (CH₃NH₃PbI₃ or MAPbI₃) — has $E \sim 17.8$ GPa, $E \sim 17.8$ GPa, and $E \sim 17.8$ GPa.

In this context, the mechanical behavior of OIHP grain boundaries are also important, because OIHP thin films used in PSCs are invariably polycrystalline due to the way they are solution-processed. While there has been reference to effect of grain size on the $G_{\rm C}$ of OIHP thin films by Rolston, *et al.*[15] there have been no systematic studies on this important topic. Furthermore, the mechanical behavior of the interfaces between OIHP thin film and the adjacent functional layers needed in PSCs, such as electron-transport layer (ETL) or hole-transport layer (HTL), is equally important. Here we have characterized the fracture behavior, and measured the $G_{\rm C}$ values, of MAPbI₃ thin films with two different average grain sizes. We find that fracture in thin films with an average grain size (~290 nm) smaller than the typical film thickness (~500 nm) occurs within the MAPbI₃ thin film intergranularly, with a low $G_{\rm C}$ of 0.41±0.17 J.m⁻². In contrast, when the average grain size (~840 nm) is larger than the film thickness, fracture is forced to occur along the interface between MAPbI₃ and the ETL, resulting in a much higher $G_{\rm C}$ of 1.14±0.24 J.m⁻².

However, these values are still much lower than that of single-crystal MAPbI₃ $G_{\rm C}$ of ~2.7 J.m⁻².[14]

The glass substrates (microscope slides, $37.5 \times 12.5 \times 1 \text{ mm}^3$) used in this study were coated with a thin layer (~25 nm) of SnO₂, a commonly used ETL in PSCs, using a process described elsewhere.[22] The MAPbI₃ thin films (~500 nm thickness) were solution-deposited on the ETLcoated glass substrates using the 'solvent-engineering' method. [23] Briefly, the precursor solution was prepared by dissolving 159 mg of MAI (Greatcell, Australia) and 461 mg of PbI₂ (Sigma-Aldrich, USA) in 620 mg of N,N-dimethylformamide (DMF; Acros Organics, USA) to obtain a 50 wt% solution. The solution was then spin-coated at 4000 rpm for 20 s total. At the 7th second of spinning, 250 µL of the anti-solvent chlorobenzene (Sigma-Aldrich, USA) was dripped at the center. The as-coated wet film was then annealed at 120 °C for 10 min on a hot-plate (uncovered) to obtain fine-grained MAPbI₃ thin films. To obtain coarse-grained MAPbI₃ thin films, the 'solvent-annealing' method was used.[24, 25] Here, the as-coated wet film was covered by an inverted Petri dish and annealed at 120 °C for 20 min on the hot-plate, where a 10 µL drop of dimethyl sulfoxide (DMSO; Acros Organics, USA) was placed near the substrate under the Petri dish. Subsequently, the as-processed surfaces of both types of MAPbI₃ thin films were coated with thin layer (~160 nm) of polymethylmethacrylate (PMMA) for protection. This was accomplished by spin-coating 80 µL of a 10 wt% PMMA (Sigma-Aldrich, USA) solution in chlorobenzene at 4000 rpm for 20 s while not damaging the MAPbI₃ thin film. This was allowed to dry at room temperature for 30 min. All the afore-mentioned steps were performed in a N₂-filled glovebox. A thin layer of epoxy (Hysol, USA) was then applied onto the PMMA layer to 'glue' another cleaned glass substrate on top. The 'sandwich' double cantilever beam (DCB) specimens were then cured in a drybox for 12 h, and the excess epoxy at the edges was cleaned off with a razor blade before mechanical testing.

The DCB specimens were tested using a method described elsewhere.[15] Briefly, a planar crack was introduced along the width (B = 12.5 mm) dimension of the specimen by inserting a razor blade into the 'sandwich.' Aluminum tabs were glued to the glass substrates on either side of the 'sandwich' specimen at the cracked end of the long dimension (37.5 mm). The cracked DCB specimens were loaded in tension to 'peel' the specimen apart using a Delaminator apparatus (DTS, USA). A constant displacement rate of 0.4 μ m.s⁻¹ was used, and the load (P) - displacement (Δ)

response was recorded during loading. The crack length (a) of the DCB sample was estimated using the compliance method in conjunction with the following relation:[15]

$$a = \left(\frac{d\Delta}{dP} * \frac{BEh^3}{8}\right)^{\frac{1}{3}} - 0.64h,\tag{1}$$

where B (= 12.5 mm) and E (= 70 GPa) are the width and the Young's modulus of the glass substrate, respectively, and h (= 1 mm) is the half-thickness of the DCB specimen (all the layers in the 'sandwich' are much too thin and are neglected). The toughness G_C is then given by the relation:[15]

$$G_{\rm C} = \frac{12P_{\rm C}^2 a^2}{B^2 E h^3} (1 + 0.64 \frac{h}{a})^2, \tag{2}$$

where $P_{\rm C}$ is the peak load at failure. Five DCB specimens were tested for each grain size, and the average $G_{\rm C}$ and the standard deviation values are reported for each set.

Scanning electron microscopes (SEMs; LEO 1530 VP, Zeiss, Germany or Quattro ESEM, ThermoFisher Scientific, USA) were used to observe top surfaces of the as-processed fine-grained and coarse-grained MAPbI₃ thin films. The grain sizes were determined using the linear-intercept method on the SEM images, in conjunction with the ImageJ image-analysis software, where ~100 grains were used for each set of materials. Note that the naturally formed grooves were assumed to represent the grain boundaries, which can lead to some overestimation of the grain size in OIHP thin films.[26, 27] The mating fracture surfaces of the failed DCB specimens after mechanical testing were also observed in the SEM. X-ray diffraction (Discovery D8, Bruker, Germany) was performed on the top surfaces of the as-processed MAPbI₃ thin films, and the mating fracture surfaces.

Figures 1A and 2A show SEM images of the top surfaces of as-processed fine-grained and coarse-grained MAPbI₃ thin films with estimated average grains sizes of ~290 nm and ~840 nm, respectively. The indexed XRD patterns in Figs. S1A and S1B in Supplementary Material (SM) confirm single-phase MAPbI₃ in both the fine-grained and coarse-grained thin films, respectively.

Figures 1B and 1C are SEM image and photograph, respectively, of the fracture surface of the top half of the fine-grained DCB specimen after failure. The presence of MAPbI₃ is clearly seen (appears dark visually), which is confirmed by the XRD pattern in Fig. S1A in SM. Similarly, Figs. 1D, 1E, and S1A confirm the presence of MAPbI₃ on the mating fracture surface on the bottom side of the failed fine-grained DCB specimen. This indicates that fracture in the fine-grained DCB specimen occurs within the MAPbI₃ thin film, and the grain-size scale roughness observed in the

SEM images in Figs. 1B and 1D indicates intergranular fracture. This is depicted schematically (cross-section) in Fig. 1F. The corresponding G_C is measured to be 0.41 ± 0.17 J.m⁻² (Fig. 3), and it represents the grain-boundary toughness (cohesion) of the fine-grained MAPbI₃ thin film.

Figures 2B and 2C are SEM image and photograph, respectively, of the fracture surface of the top half after failure of the coarse-grained DCB specimen, showing relatively smoother fracture surface. The presence of MAPbI₃ is clearly seen, which is confirmed by the XRD pattern in Fig. S1B in SM. In contrast, Figs. 2D, 2E, and S1B indicate little presence of MAPbI₃ on the smooth mating fracture surfaces on the bottom side of the failed coarse-grained DCB specimen. These results indicate that the failure has occurred at the MAPbI₃/SnO₂ interface in this case, as depicted schematically (cross-section) in Fig. 2F. The corresponding G_C is almost three times higher at 1.14 ± 0.24 J.m⁻² (Fig. 3), and it represents the toughness (adhesion) of the MAPbI₃/ETL interface. This failure mode is attributed to the fact that, unlike the fine-grained thin films, 'horizontal' lower-toughness grain boundaries do not exist in the coarse-grained thin films, thereby forcing the facture to occur along the next weakest path, *i.e.* the MAPbI₃/SnO₂ interface.

Bending experiments were also performed, where the fine-grained and coarse-grained MAPbI₃ thin films were also deposited using the same procedure as above, but on flexible polyethylene terephthalate (PET) polymer substrates (15×10 mm², ~178 µm thickness) coated with indiumdoped tin oxide (ITO; ~100 nm thickness) transparent-conducting oxide (obtained commercially; Sigma Aldrich, USA). These specimens were bent around a glass mandrel of radius 7.4 mm with the MAPbI₃ film on the outside (tension), using a procedure described elsewhere.[16] The specimens, while being bent (Fig. 4C), were observed inside the SEM. Figures 4A and 4B are top-surface SEM images of fine-grained and coarse-grained MAPbI₃ thin films, respectively, showing intergranular 'channeling' cracks, which is depicted schematically in Fig. 4C for the coarse-grain case. The intergranular nature of fracture in the fine-grained thin film is not surprising as the grain-boundary toughness is significantly lower than the single-crystal toughness (Fig. 3). But importantly, these results show that grain boundaries in both fine-grained and coarse-grained thin films are equally weak. This support the above argument that the interfacial fracture in the coarse-grained DCB specimen (Fig. 2) occurs because of the paucity of 'horizontal' grain boundaries.

The results from this study clearly highlight, for the first time, the benefit of larger grains in improving the overall fracture resistance of OIHP thin films for PSCs, and thereby the reliability. This is consistent with the general improvements observed in both the performance and stability

of PSCs by increasing the grain size, and decreasing the grain-boundary density, in OIHP thin films.[6, 26, 28-31] This is largely due to: (i) reduction in photocarriers scattering, (ii) fewer recombination sites, and (iii) limit on ingression of environmental species.

Acknowledgement

The financial support for this research from the Office of Naval Research (grant# N00014-17-1-2232) and the National Science Foundation (grant# OIA-1538893). The authors thank N. Rolston for helpful discussions.

References

- [1] N.-G. Park, M. Grätzel, T. Miyasaka. Organic-Inorganic Halide Perovskite Photovoltaics: From Fundamentals to Device Architectures. Zurich, Switzerland: Springer, 2016.
- [2] H.J. Snaith, Nature Mater. 17 (2018) 372.
- [3] A.K. Jena, A. Kulkarni, T. Miyasaka, Chem. Rev. 119 (2019) 3026.
- [4] A. Kojima, K. Teshima, Y. Shirai, T. Miyasaka, J. Am. Chem. Soc. 131 (2009) 6050.
- [5] NREL, https://www.nrel.gov/pv/cell-efficiency.html (2019)
- [6] W.A. Dunlop-Shohl, Y. Zhou, N.P. Padture, D.B. Mitzi, Chem. Rev. 119 (2019) 3193.
- [7] M. Kaltenbrunner, G. Adam, E.D. Głowacki, M. Drack1, R. Schwödiauer, L. Leonat, D.H. Apaydin, H. Groiss, M.C. Scharber, M.S. White, N.S. Sariciftci, S. Bauer, Nature Mater. 14 (2015) 1032.
- [8] D. Yang, R. Yang, S. Priya, S. Liu, Angew. Chem. Intl. Ed. 58 (2019) 4466.
- [9] Q. Dong, J. Li, Y. Shi, M. Chen, L.K. Ono, K. Zhou, C. Zhang, Y. Qi, Y. Zhou, N.P. Padture, L. Wang, Adv. Ener. Mater. 9 (2019) 1900834.
- [10] T.C. Sum, N. Mathews. Halide Perovskites: Photovoltaics, Light Emitting Diodes and Beyond. Weinheim, Germany: Wiley-VCH, 2019.
- [11] Y. Rong, Y. Hu, A. Mei, H. Tran, M.I. Saidaminov, S.I. Seok, M. McGehee, E.H. Sargent, H. Han, Science 361 (2018) 1214.
- [12] C.C. Boyd, R. Cheacharoen, T. Leijtens, M.D. McGehee, Chem. Rev. 119 (2019) 3418.
- [13] N. Rolston, B.L. Watson, C.D. Bailie, M.D. McGehee, J.P. Bastos, R. Gehlhaar, J.-E. Kim, D. Vak, A.T. Mallajosyula, G. Gupta, A.D. Mohite, R.H. Dauskardt, Extreme Mech. Lett. 9 (2016) 353.

- [14] C. Ramirez, S.K. Yadavalli, H.F. Garcces, Y. Zhou, N.P. Padture, Scripta Mater. 150 (2018) 36.
- [15] N. Rolston, A.D. Printz, J.M. Tracy, H.C. Weerasinghe, D. Vak, L.J. Haur, A. Priyadarshi, N. Mathews, D.J. Slotcavage, M.D. McGehee, R.E. Kalan, K. Zielinski, R.L. Grimm, H. Tsai, W. Nie, A.D. Mohite, S. Gholipour, M. Saliba, M. Grätzel, R.H. Dauskardt, Adv. Ener. Mater. 8 (2018) 1702116.
- [16] S.K. Yadavalli, Z. Dai, H. Zhou, Y. Zhou, N.P. Padture, Acta Mater. 187 (2020) 112.
- [17] J. Feng, APL Mater. 2 (2014) 081801.
- [18] Y. Rakita, S.R. Cohen, N.K. Kedem, G. Hodes, D. Cahen, MRS Comm. 5 (2015) 623.
- [19] S. Sun, F.H. Isikgor, Z. Deng, F. Wei, G. Kieslich, P.D. Bristowe, J. Ouyang, A.K. Cheetham, ChemSusChem 10 (2017) 3740.
- [20] M.A. Reyes-Martinez, A.L. Abdelhady, M.I. Saidaminov, D.Y. Chung, O.K. Bakr, M.G. Kanatzidis, W.O. Soboyejo, Y.-L. Loo, Adv. Mater. 29 (2017) 1606556.
- [21] L.-J. Li, S.-J. Sun, Y. Qin, K. Li, W. Li, Coord. Chem. Rev. 391 (2019) 15.
- [22] Q. Jiang, L. Zhang, W. H, X. Yang, J. Meng, H. Lu, Z. Yin, J. Wu, X. Zhang, Nature Ener. 2 (2016) 16177.
- [23] N.J. Jeon, J.H. Noh, Y.C. Kim, W.S. Yang, S. Ryu, S.I. Seok, Nature Mater. 9 (2014) 897.
- [24] Z.G. Xiao, Q.F. Dong, C. Bi, Y.C. Shao, Y.B. Yuan, J.S. Huang, Adv. Mater. 26 (2014) 6503.
- [25] S.K. Yadavalli, Y. Zhou, N.P. Padture, ACS Ener. Lett. 3 (2018) 63.
- [26] Y. Zhou, O.S. Game, S. Pang, N.P. Padture, J. Phys. Chem. Lett. 6 (2015) 4827.
- [27] G.W.P. Adhyaksa, S. Brittman, H. Āboliņš, A. Lof, X. Li, J.D. Keelor, Y. Luo, T. Duevski, R.M.A. Heeren, S.R. Ellis, D.P. Fenning, E.C. Garnett, Adv. Mater. 30 (2018) 1804792.
- [28] M. Yang, Y. Zhou, Y. Zeng, C.-S. Jiang, N.P. Padture, K. Zhu, Adv. Mater. 27 (2015) 6363.
- [29] Y. Yuan, J. Huang, Acc. Chem. Res. 49 (2016) 286.
- [30] F. Ji, S. Pang, L. Zhang, Y. Zong, G. Cui, N.P. Padture, Y. Zhou, ACS Ener. Lett. 2 (2017) 2727.
- [31] S.K. Yadavalli, Z. Dai, M. Hu, Q. Dong, W. Li, Y. Zhou, R. Zia, N.P. Padture, Acta Mater. in press (2020).

Figure Captions

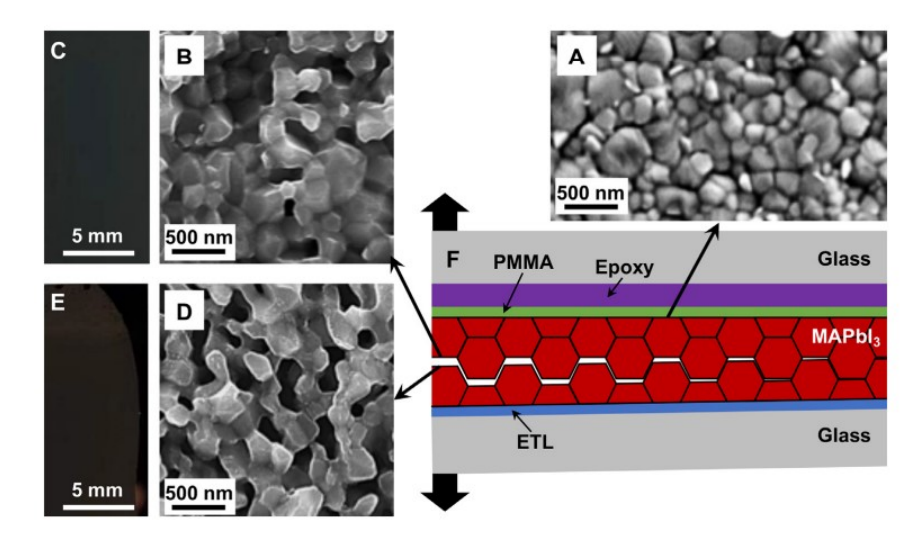


Figure 1. SEM images of: (A) top surface of as-processed fine-grained MAPbI₃ thin film, (B) top fracture surface, and (D) bottom fracture surface. Corresponding photographs of fracture surfaces: (C) top and (E) bottom. (F) Cross-sectional schematic diagram showing DCB specimen with intergranular mode of fracture. Not to scale.

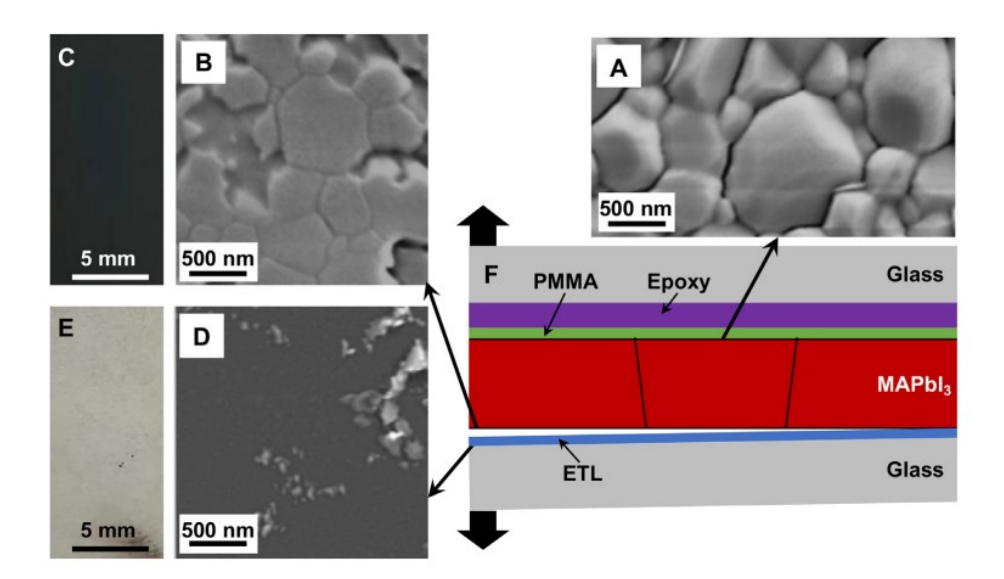


Figure 2. SEM images of: (A) top surface of as-processed coarse-grained MAPbI₃ thin film, (B) top fracture surface, and (D) bottom fracture surface. Corresponding photographs of fracture surfaces: (C) top and (E) bottom. (F) Cross-sectional schematic diagram showing DCB specimen with interfacial mode of fracture. Not to scale.

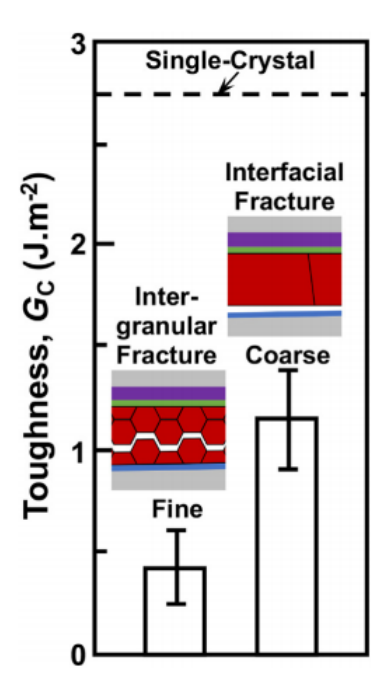


Figure 3. The toughness of fine-grained MAPbI₃ thin film and MAPbI₃/ETL interface in coarse-grained MAPbI₃ thin film. Average and standard deviation of five measurements for each material. The single-crystal value from Ref. [14] is marked.

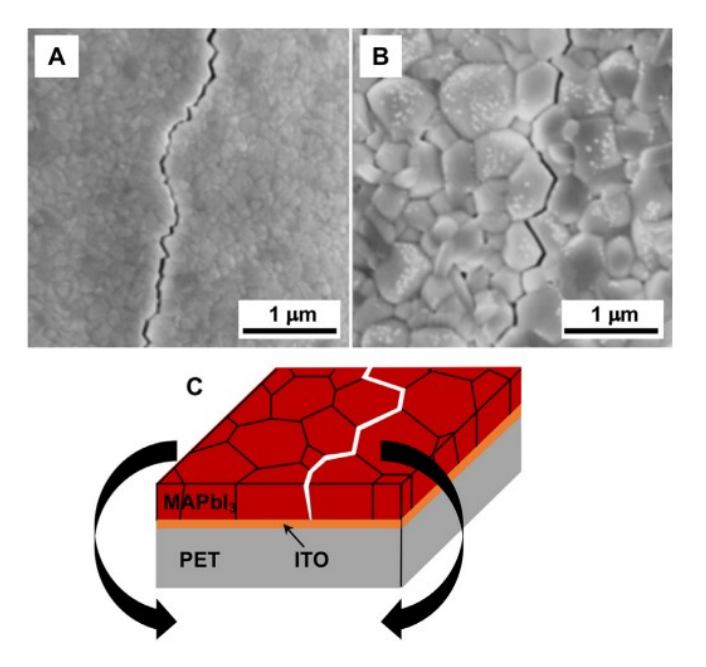


Figure 4. Top-surface SEM images of fractured MAPbI₃ thin films on flexible ITO-coated PET substrates under bending: (A) fine-grained and (B) coarse-grained. (C) Schematic diagram illustrating intergranular 'channeling' crack in the coarse-grain thin film. Not to scale.